# Six lanthanide(III) coordination polymers with 3,5-bis(4'-carboxy-phenyl)-1,2,4-triazole: syntheses, structures, and photoluminescence

Xiangyang Hou, Xiao Wang, Hao Wang, Loujun Gao, Feng Fu, Jijiang Wang, Long Tang & Jia Cao

Taylor & Francis
Taylor & Francis Group

# Six lanthanide(III) coordination polymers with 3,5-bis (4′-carboxy-phenyl)-1,2,4-triazole: syntheses, structures, and photoluminescence

XIANGYANG HOU*, XIAO WANG, HAO WANG, LOUJUN GAO, FENG FU,
JIJIANG WANG, LONG TANG and JIA CAO

Department of Chemistry and Chemical Engineering, Shaanxi Key Laboratory of Chemical Reaction
Engineering, Yan'an University, Yan'an, China
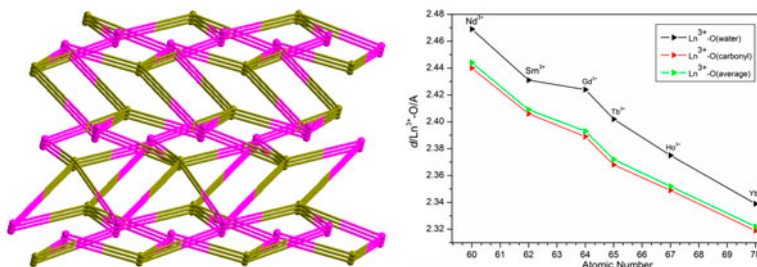
Six 3-D lanthanide(III)-metal-organic frameworks (MOFs) through multidentate 3,5-bis(4′-carboxy-phenyl)-1,2,4-triazole ($H_2BCPT$); acetic acid (HOAc); and corresponding trivalent rare earth chloride, $\{[Ln(BCPT)(OAc)(H_2O)]\cdot(H_2O)\}_n$ (Ln = $Nd^{3+}$ (**1**); $Sm^{3+}$ (**2**); $Gd^{3+}$ (**3**), $Tb^{3+}$ (**4**), $Ho^{3+}$ (**5**), $Yb^{3+}$ (**6**)), have been synthesized. MOFs **1–6** were characterized via FT-IR spectroscopy, elemental analysis, X-ray single-crystal diffraction, thermal analysis, and fluorescence. MOFs **1–6** are isomorphous, which can be described as a 3-D construction containing a dinuclear cluster [$Tb_2(CO_2)_2(O)_2$]. The 3-D structure with (4,4) topologies have been extended through $BCPT^{2-}$ using $\mu_4$-$kO;kO;kO;kO$ coordination modes. Solid-state luminescence of **1–4** and **6** shows the characteristic bands of $Nd^{3+}$, $Sm^{3+}$, $Tb^{3+}$, and $Yb^{3+}$ from visible to near-infrared spectral regions.

*Keywords*: Lanthanide(III)-MOFs; Structures; Photoluminescence

## 1. Introduction

The construction of high dimensional lanthanide(III)-MOFs are interesting for architectures and potential application as function materials, such as luminescence and porosity properties [1]. Many $Ln^{3+}$-MOFs exhibiting fascinating structures and various photophysical properties have been synthesized [2]. $Sm^{3+}$, $Eu^{3+}$, $Gd^{3+}$, $Tb^{3+}$, $Dy^{3+}$, and $Tm^{3+}$ ions can produce

*Corresponding author. Email: wangxiaosun@yau.edu.cn

luminescence properties in the visible region, and $Nd^{3+}$, $Pr^{3+}$, $Er^{3+}$, and $Yb^{3+}$ are able to generate luminescence properties in the near-infrared region, attributed to f–f transitions of $Ln^{3+}$-MOFs with relatively narrow bandwidth [3]. However, $Ln^{3+}$ ions usually give weak luminescence, due to spin and Laporte forbidden f–f electronic transitions [4]. The method to solve this problem is to introduce antenna chromophores with strong absorption coefficient. An organic ligand with a triplet excited state serves as antenna chromophore to efficiently transfer absorbed energy to $Ln^{3+}$ ions. The energy transfer process is called the "antenna effect" [5]. Hence, a number of chromophoric antenna ligands were used effectively as sensitizer to stimulate $Ln^{3+}$ ion luminescence, especially hydroxyquinoline carboxylate ligands [6], carboxylate ligands [7], β-diketonate [8], phosphonates [9] and sulfonates [10]. Rare earth ions have diverse, variable, high coordination numbers and flexible changeable coordination environments, which makes the MOF structures interesting.

Recently, we have focused on a multidentate ligand with hybrid oxygen–nitrogen donors, $H_2BCPT$, in which the large л-conjugated system of the benzimidazole is expected as an effective chromophore for lanthanide luminescence. Second, $H_2BCPT$ adopts various coordination modes when it coordinates to metals and may produce various structures, owing to its carboxylate and triazole arms. Third, the introduction of a small bridging ligand to obtain a dinuclear cluster system is one of the common ways to obtain higher dimensional networks, and acetate has been used for this purpose. In this contribution, six 3-D $Ln^{3+}$-MOFs, $\{[Ln(BCPT)(OAc)(H_2O)]·(H_2O)\}_n$ (Ln = $Nd^{3+}$ (**1**); $Sm^{3+}$ (**2**), $Gd^{3+}$ (**3**), $Tb^{3+}$ (**4**), $Ho^{3+}$ (**5**), $Yb^{3+}$ (**6**)), were hydrothermally synthesized and characterized. The fluorescence properties of **1**–**4** and **6** in the solid state were investigated. To the best of our knowledge, **1**–**6** are the first instances of $Ln^{3+}$-MOFs constructed with $H_2BCPT$ ligands.

## 2. Experimental

### 2.1. *Materials and methods*

Solvents and starting materials of analytical grade in the experiments were purchased from Sigma–Aldrich and used without purification. Elemental analyses (C, H, and N) were determined on a Perkin–Elmer 2400 type elemental analyzer. The infrared spectra were measured between 4000 and 400 $cm^{-1}$ on a Bruker EQUINOX-55 spectrophotometer using KBr pellets. Typical PXRD patterns were recorded using Cu Kα (45 kV, 40 mA, $\lambda = 1.542$ Å) radiation on a PANalytical X'Pert PRO diffractometer. The UV absorption studies were carried out with a Shimadzu UV-2450 spectrophotometer. Thermogravimetric analyses were performed in platinum crucibles on a NETZSCH STA449C thermogravimetric analyzer between room temperature and 900 °C with a heating rate of 10 °C·$min^{-1}$. Solid sample photoluminescence analyses were performed on an Edinburgh Instrument FLS920 fluorescence spectrometer at ambient temperature.

### 2.2. *Syntheses of $\{[Ln(BCPT)(OAc)(H_2O)]·(H_2O)\}_n$ (Ln = $Nd^{3+}$ (1); $Sm^{3+}$ (2), $Gd^{3+}$ (3), $Tb^{3+}$ (4), $Ho^{3+}$ (5), $Yb^{3+}$ (6))*

The $Na_2BCPT·2.77$ ($H_2O$) is prepared by the addition of two equivalents of sodium hydroxide to a suspension of $H_2BCPT$ acid in deionized water. The mixture is stirred and refluxed for 30 min. After filtration and drying, a white powder of $Na_2BCPT·2.77(H_2O)$ is

collected, which is characterized by elemental analysis (found: H, 3.31; C, 47.67; N, 10.75; Calcd: H, 3.64; C, 47.67; N, 10.42). Weighed amounts of $NdCl_3 \cdot 6H_2O$ (*m*: 0.0179 g, *n*: 0.05 mmol), $Na_2BCPT \cdot 2.77$ ($H_2O$) (*m*: 0.0367 g, *n*: 0.09 mmol) and HOAc (*m*: 0.0072 g, *n*: 0.12 mmol) are dissolved in 10 mL deionized water. The mixing solution materials are stirred for an hour at room temperature and which sealed in a 25 mL Teflon-lined stainless steel autoclave reactor under autogenous pressure at 130 °C about 120 h. The reaction system was cooled to 20 °C at 3 °C·h$^{-1}$. Colorless sheet-shaped crystals have been collected by filtration, washed by deionized water, and dried under air. Yield 0.0156 g (57%, based $Nd^{3+}$). C, H, N percentage analysis (%): $C_{18}H_{16}N_3O_8Nd$ (**1**), Calcd: H, 2.95; C, 39.55; N, 7.69. Found: H, 3.01; C, 39.47; N, 7.65. IR: 3447m, 2938w, 1632s, 1574s, 1537m, 1476m, 1419m, 1138w, 1018w, 745w. The same method as for **1** is used to synthesize **2–6** with $SmCl_3 \cdot 6H_2O$ (*m*: 0.0182 g, *n*: 0.05 mmol), $GdCl_3 \cdot 6H_2O$ (*m*: 0.0186 g, *n*: 0.05 mmol), $TbCl_3 \cdot 6H_2O$ (*m*: 0.0187 g, *n*: 0.05 mmol), $HoCl_3 \cdot 6H_2O$ (*m*: 0.0190 g, *n*: 0.05 mmol), and $YbCl_3 \cdot 6H_2O$ (*m*: 0.0194 g, *n*: 0.05 mmol) instead of $NdCl_3 \cdot 6H_2O$. Colorless or pink sheet-shaped crystals of **2–6** were collected in 0.0185 g (67%), 0.0193 g (69%), 0.0132 g (47%), 0.0167 g (59%), and 0.0173 g (60%) yield based on $Sm^{3+}$, $Gd^{3+}$, $Tb^{3+}$, $Ho^{3+}$, and $Yb^3$, respectively. C, H, N percentage analysis (%): $C_{18}H_{16}N_3O_8Sm$ (**2**), Calcd: H, 2.92; C, 39.12; N, 7.60. Found: H, 2.98; C, 39.13; N, 7.56. IR: 3442m, 2927w, 1619s, 1597s, 1545m, 1493m, 1418m, 1127w, 1031w, 757w. $C_{18}H_{16}N_3O_8Gd$ (**3**), Calcd: H, 2.88; C, 38.64; N, 7.51. Found: H, 2.85; C, 38.77; N, 7.62. IR: 3436m, 2927w, 1619s, 1597s, 1578m, 1545m, 1413m, 1145w, 1066w, 741w. $C_{18}H_{16}N_3O_8$ Tb (**4**) Calcd: H, 2.87; C, 38.52; N, 7.49. Found: H, 2.92; C, 38.56; N, 7.48. IR: 3442m, 2911w, 1614s, 1574s, 1466m, 1425m, 1134m, 1008w, 752w. $C_{18}H_{16}N_3O_8Ho$ (**5**), Calcd: H, 2.84; C, 38.11; N, 7.41. Found: H, 2.89; C, 38.16; N, 7.32. IR: 3447m, 2916w, 1626s, 1578s, 1482m, 1418m, 1128m, 735w. $C_{18}H_{16}N_3O_8Yb$ (**6**) Calcd: H, 2.80; C, 37.57; N, 7.30. Found: H, 2.84; C, 37.82; N, 7.33. IR: 3431m, 2933w, 1619s, 1568s, 1488s, 1408m, 1138m, 1018m, 717w.

## 2.3. *X-ray crystal structure determination*

Appropriate single crystals of MOFs **1–6** were selected and mounted on glass fibers for data collection. Crystallographic data were carried out on a Bruker Apex II CCD diffractometer with graphite-monochromated MoKα radiation ($\lambda = 0.71073$ Å). All absorption corrections were applied using the multiscan program SADABS [11]. All structures were solved by direct methods using SHELXS-97 of the SHELXTL package and refined by full-matrix least-squares method with SHELXTL-97 [12]. All non-hydrogen atoms in the seven structures were found from the difference Fourier map and refined with anisotropic displacement parameters. The hydrogens (H–C and H–N) of organic ligands were generated geometrically and included in idealized positions using a riding model and refined isotropically. The hydrogens (H–O) of coordination and solvent waters were located from the difference Fourier maps, restrained at fixed positions and refined isotropically. A summary of the crystallographic data and parameters for **1–6** is listed in table 1. Selected bond lengths are collected in table 2 and table S1 (see online supplemental material at http://dx.doi.org/10.1080/00958972.2015.1025768). Crystallographic data for the structural analysis have been deposited with the Cambridge Crystallographic Data Center, CCDC No. 999810-999815 for **1–6**. Copies of this information may be obtained free of charge on application to CCDC, 12 Union Road, Cambridge CB2 1EZ, UK (Fax: +44 1223 336 033; E-mail: deposit@ ccdc.cam.ac.uk or http://www.ccdc.cam.ac.uk).

Table 1.  Crystal data and structure refinement summary for **1–6**.

| Compound | **1** | **2** | **3** |
|---|---|---|---|
| $T$ (K) | 293(2) | 296(2) | 296(2) |
| Empirical formula | $C_{18}H_{16}N_3O_8Nd$ | $C_{18}H_{16}N_3O_8Sm$ | $C_{18}H_{16}N_3O_8Gd$ |
| Formula weight | 546.58 | 552.70 | 559.59 |
| Crystal system | Monoclinic | Monoclinic | Monoclinic |
| Space group | $P2(1)/c$ | $P2(1)/c$ | $P2(1)/c$ |
| $a$ (Å) | 15.9866(5) | 16.0457(12) | 16.1138(7) |
| $b$ (Å) | 14.8018(3) | 14.7446(11) | 14.7294(6) |
| $c$ (Å) | 8.3195(2) | 8.2511(6) | 8.2117(3) |
| $\alpha$ (°) | 90.00 | 90.00 | 90.00 |
| $\beta$ (°) | 96.397(2) | 96.6100(10) | 96.7920(10) |
| $\gamma$ (°) | 90.00 | 90.00 | 90.00 |
| $V$ (Å$^3$) | 1956.39(9) | 1939.1(2) | 1935.34(14) |
| $D_c$ (Mg·m$^{-3}$) | 1.856 | 1.886 | 1.914 |
| $F(0\,0\,0)$ | 1068 | 1076 | 1084 |
| Reflections collected | 9351 | 11,851 | 10,618 |
| Data/restraints/ parameters | 4003/0/279 | 4628/0/271 | 3952/0/163 |
| $Z$ | 4 | 4 | 4 |
| Final $R$ | 0.0255 | 0.0315 | 0.0440 |
| $R$ indices (all data) | 0.0553 | 0.0746 | 0.1173 |
| GOF on $F^2$ | 0.969 | 1.001 | 0.956 |
| *Compound* | **4** | **5** | **6** |
| $T$ (K) | 293(2) | 296(2) | 293(2) |
| Empirical formula | $C_{18}H_{16}N_3O_8Tb$ | $C_{18}H_{16}N_3O_8Ho$ | $C_{18}H_{16}N_3O_8Yb$ |
| Formula weight | 561.27 | 567.27 | 575.38 |
| Crystal system | Monoclinic | Monoclinic | Monoclinic |
| Space group | $P2(1)/c$ | $P2(1)/c$ | $P2(1)/c$ |
| $a$ (Å) | 16.1151(6) | 16.1537(9) | 16.2421(7) |
| $b$ (Å) | 14.6839(5) | 14.6264(9) | 14.5719(6) |
| $c$ (Å) | 8.1831(3) | 8.1223(5) | 8.0697(4) |
| $\alpha$ (°) | 90.00 | 90.00 | 90.00 |
| $\beta$ (°) | 96.9280(10) | 97.1810(10) | 97.5690(10) |
| $\gamma$ (°) | 90.00 | 90.00 | 90.00 |
| $V$ (Å$^3$) | 1922.25(12) | 1904.0(2) | 1893.28(15) |
| $D_c$ (Mg·m$^{-3}$) | 1.939 | 1.979 | 2.019 |
| $F(0\,0\,0)$ | 1096 | 1104 | 1116 |
| Reflections collected | 10,540 | 10,560 | 10,494 |
| Data/restraints/ parameters | 3897/0/279 | 3892/0/311 | 3863/0/323 |
| $Z$ | 4 | 4 | 4 |
| Final $R$ | 0.0174 | 0.0237 | 0.0182 |
| $R$ indices (all data) | 0.0487 | 0.0547 | 0.0404 |
| GOF on $F^2$ | 1.108 | 1.104 | 1.031 |

## 3.  Results and discussion

### 3.1.  *Structure description of MOF 4*

MOFs **1–6** are isostructural and crystallize in a monoclinic space group $P2(1)/c$; hence, we use MOF **4** as an example for detailed discussion. As depicted in figure 1(a), the asymmetric unit of **4** contains one crystallographically independent $Tb^{3+}$, one deproto-nated carboxylic $BCPT^{2-}$, one deprotonated $OAc^-$, one aqua ligand, and one lattice water. Each $Tb^{3+}$ is eight-coordinate in a distorted bis-capped trigonal prism coordination geometry [figure 1(b)] surrounded by an $[O_8]$ donor set and coordinated by four car-boxylate oxygens (O1, O2#1, O3#2, and O4#3) from four different $BCPT^{2-}$ ligands,

Table 2. All bond lengths (Å) and angles (°) for **4**.

| Tb1–O1 | 2.306(2) | Tb1–O2#1 | 2.331(2) | Tb1–O3#2 | 2.324(2) |
|---|---|---|---|---|---|
| Tb1–O4#3 | 2.324(3) | Tb1–O6 | 2.455(3) | Tb1–O7 | 2.488(2) |
| Tb1–O7#4 | 2.385(2) | Tb1–O8 | 2.402(2) | O1–Tb1–O2#1 | 87.91(8) |
| O3#2–Tb1–O2#1 | 74.87(8) | O3#2–Tb1–O7#4 | 72.68(9) | O4#3–Tb1–O7#4 | 73.58(9) |
| O1–Tb1–O4#3 | 90.80(9) | O1–Tb1–O3#2 | 102.65(9) | O4#3–Tb1–O3#2 | 138.82(8) |
| O4#3–Tb1–O2#1 | 145.23(8) | O1–Tb1–O7#4 | 75.21(8) | O2#1–Tb1–O7#4 | 138.75(8) |
| O4#3–Tb1–O8 | 72.28(8) | O8–Tb1–O6 | 78.47(8) | O2#1–Tb1–O6 | 79.06(9) |
| O1–Tb1–O8 | 79.40(9) | O2#1–Tb1–O7 | 119.78(8) | O3#2–Tb1–O8 | 148.05(8) |
| O2#1–Tb1–O8 | 73.35(8) | O1–Tb1–O6 | 156.77(7) | O4#3–Tb1–O6 | 89.17(10) |
| O3#2–Tb1–O6 | 92.49(10) | O7#4–Tb1–O6 | 126.75(8) | O1–Tb1–O7 | 149.20(8) |
| O4#3–Tb1–O7 | 74.16(9) | O3#2–Tb1–O7 | 74.78(9) | O2#1–Tb1–O7 | 119.78(8) |
| O7#4–Tb1–O7 | 74.80(9) | O8–Tb1–O7 | 119.28(9) | O6–Tb1–O7 | 51.97(7) |

Note: Symmetry codes: #1: $x$, $0.5 - y$, $0.5 + z$; #2: $1 - x$, $-y$, $1 - z$; #3: $-1 + x$, $y$, $-1 + z$; #4: $-x$, $-y$, $-z$.
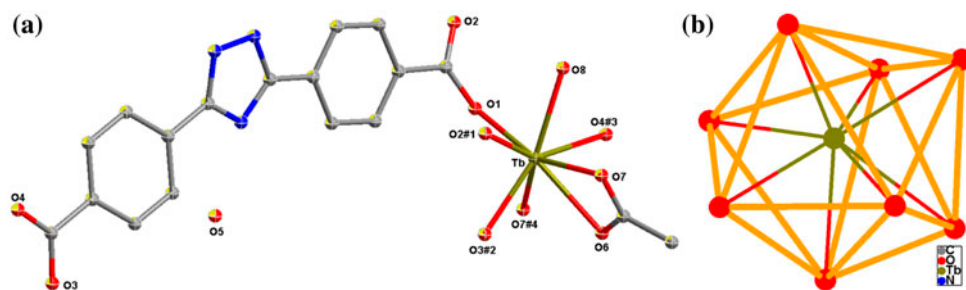


Figure 1. (a) Coordination environment of $Tb^{3+}$ in **4** at 30% probability level; (b) the distorted triangle prism coordination geometry of $Tb^{3+}$ in **4**. Symmetry codes: #1: $x$, $0.5 - y$, $0.5 + z$; #2: $1 - x$, $-y$, $1 - z$; #3: $-1 + x$, $y$, $-1 + z$; #4: $-x$, $-y$, $-z$.

three oxygens (O6, O7, and O7#4) from two different OAc⁻ ligands, and one aqua (O8) ligand. The $Tb^{3+}$–O distances from carboxylates are 2.306(2), 2.331(2), 2.324(2), 2.324 (3), 2.455(3), 2.488(2), and 2.385(2), respectively. The $Tb^{3+}$–O8 (water) distance is 2.402(2) Å. The average $Tb^{3+}$–$O_{carboxylate}$ and all $Tb^{3+}$–O bond lengths are 2.372 and 2.377 Å, respectively. All bond lengths and angles of **4** are within normal ranges, comparable to reported $Tb^{3+}$-carboxylate compounds [13]. The variation relationship between $Ln^{3+}$–O bond lengths and the atomic number of rare earth ions for **1–6** is shown in figure 2, where $Ln^{3+}$–O bonds contain averages. As a result, MOFs **1–6** reflect the lanthanide contraction.

As shown in figure 3, Tb1 and its corresponding centrosymmetric-generated atom are joined by two $\mu_2$-kO:kO carboxylate groups (O3–C16–O4) from two different $BCPT^{2-}$ ligands and two $\mu_2$-kO,O oxygen atoms (O7) from two different OAc⁻ ligands to form a $[Tb_2(CO_2)_2(O)_2]$ binuclear motif with the Tb···Tb separation of 3.8716(2) Å. The binuclear unit is centrosymmetric with Tb1, O7, Tb1, O7 on the same plane and Tb1, O3, C20, O4, Tb1, O3, C20, O4 on another plane; the angle between the planes is 89.37°. The Tb1–O7, Tb1–O3, and Tb1–O4 are 2.488(2), 2.385(2), 2.324(2), and 2.324(3) Å, and bond angles of O7–Tb1–O7 and O3–C20–O4 are 105.21 and 125.19°, respectively. [Tb(2,5-pdco) (CH₃COO)(H₂O)] [14] also contains the dinuclear unit $[Tb_2(CO_2)_2(O)_2]$ (figure S1, 2,5-H₂pdco = pyridyl-2,5-dicarboxylic acid N-oxide). The Tb···Tb, Tb–O2a, Tb–O2b separation for $[Tb_2(CO_2)_2(O)_2]$ of [Tb(2,5-pdco)(CH₃COO)(H₂O)] are 3.9964(2), 2.4898(21),
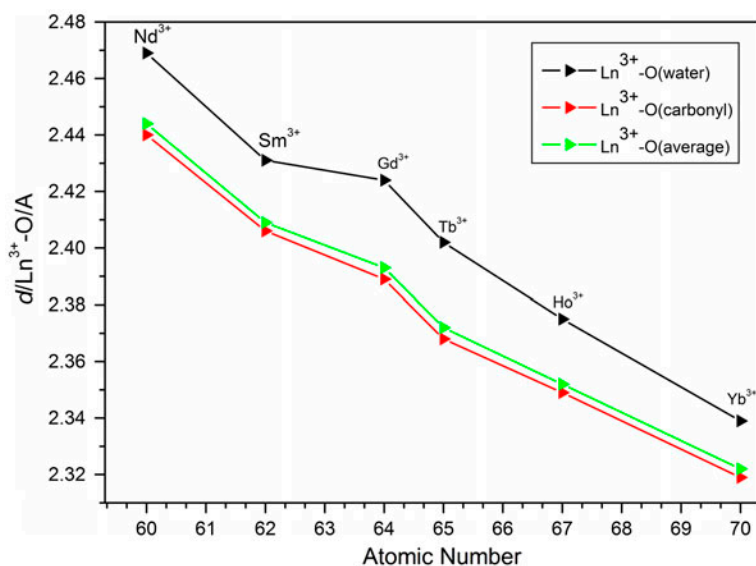
Figure 2. Profiles of the bond lengths between the $Ln^{3+}$ and the carbonyl oxygens and coordination waters *vs.* the atomic number of $Ln^{3+}$.
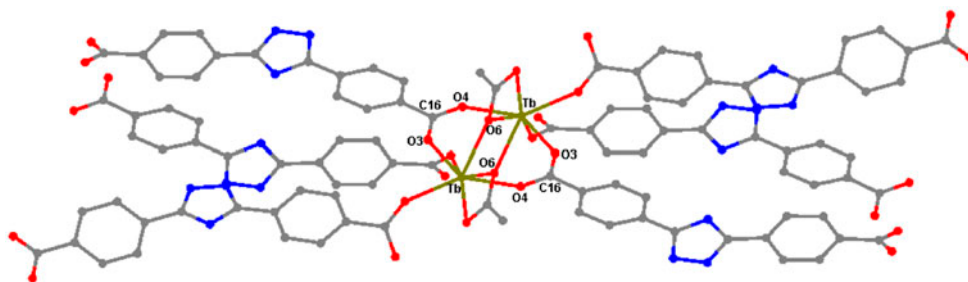


Figure 3. The binuclear unit in **4**.

2.3971(24), 2.4898(21), and 2.3971(24) Å, and two bond angles of O6a–Tb–O5b and O5a–C11a–O6a are 139.239(74) and 127.196(29)°, respectively. The binuclear unit of **4** plays an important role in expanding the complex structure. Each binuclear unit $[Tb_2(CO_2)_2(O)_2]$ is linked via carboxylate groups (O1–C1–O2) with $\mu_2$-kO:kO fashion to generate a 1-D chain along the *a* and *b* axis directions, respectively (figure 4). The Tb⋯Tb distance of the 1-D chains is 5.6573(3) Å. The dinuclear unit of $[Tb_2(CO_2)_2(O)_2]$ of [Tb (2,5-pdco)($CH_3COO$)($H_2O$)] [14] is linked via $\mu_2$-kO:kO carboxylate groups (O7a–C7a–O9a) to generate a 1-D chain along the *b* axis direction with the Tb⋯Tb distance of 5.8204(2) Å. Each binuclear unit $[Tb_2(CO_2)_2(O)_2]$ of **4** is also surrounded by four $BCPT^{2-}$ ligands through four $\mu_2$-kO:kO carboxylate groups (O1–C1–O2) to form a 2-D construction in the *b*, *c*-plane (figure 5). Obviously, the 2-D structure is formed from the binuclear unit $[Tb_2(CO_2)_2(O)_2]$. Finally, each binuclear unit is further connected by $\mu_4$-kO:kO:kO:kO $BCPT^{2-}$ [figure 14(a)] to give the 3-D framework (figure 6) of **4**. As observed in figure 6,
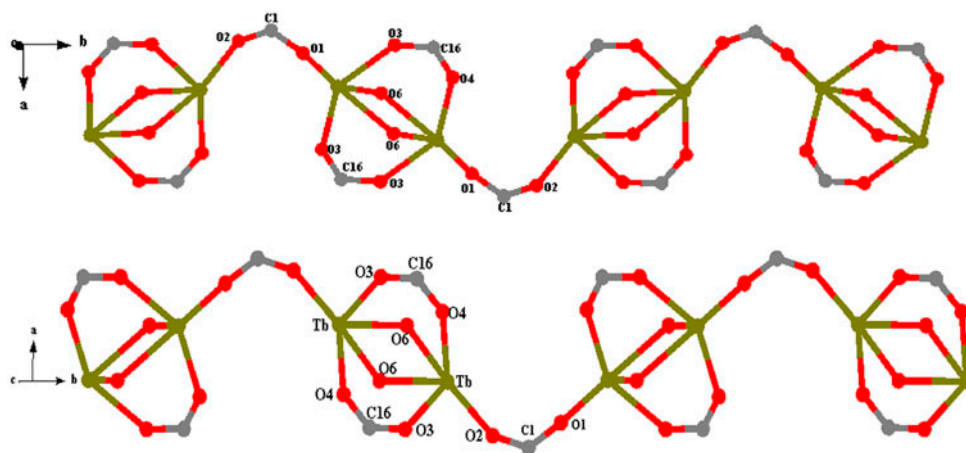
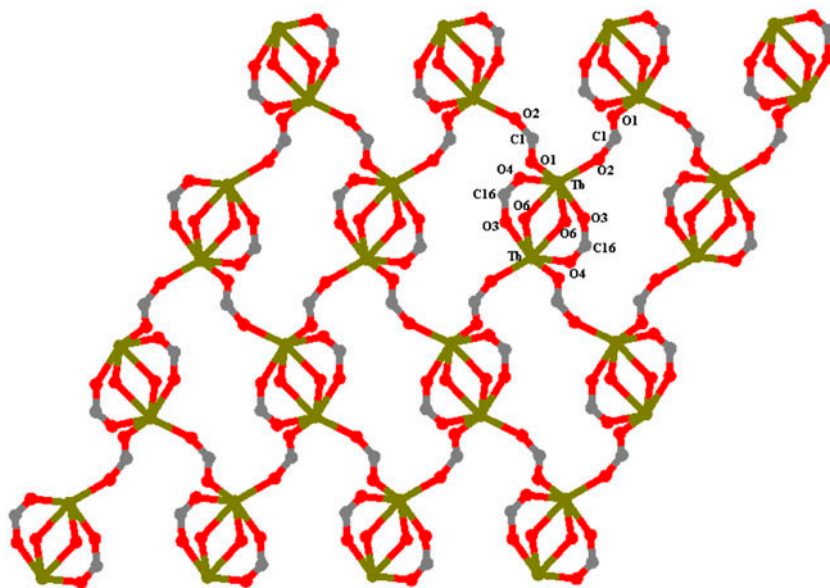Figure 4.    The 1-D chains along the *b* and *c* axes.



Figure 5.    2-D network of **4** in the *bc*-plane.

there are two larger volume holes for **4**, but their potential porosities are rather low. The void volume of the channels without the guest molecules, calculated by PLATON, is 4.4%. A noticeable weak interaction in **4** is the hydrogen bonds. The coordinated water (O8), lattice water (O5), and nitrogens (N1, N2, and N3) of BCPT$^{2-}$ form intermolecular hydrogen bonds, O5#6–H5A···N1, O5#7–H5B···N3, O(8)–H(8B)···O(4)#5, and N(2)–H(2A)···O(5). The geometrical parameters of the hydrogen bonds in **4** are summarized in table 3. The hydrogen bonds are of the type O/N–H(donor)–O/N(acceptor), which can further increase the structure stability **4**. The OAc$^{-}$ ligands merely provide oxygens via $\mu_2$-kO:kO,O
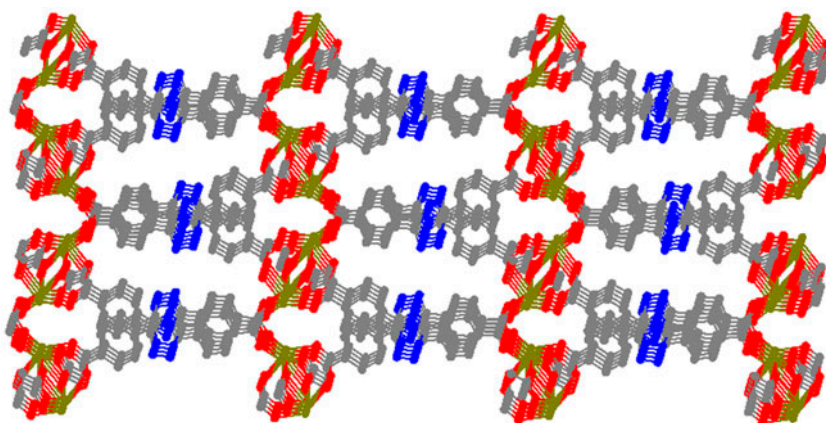
Figure 6.    3-D network of **4**.

Table 3.    Hydrogen bonds in **4**.

| Donor–H···Acceptor | $d$(D–H)/Å | $d$(H···A)/Å | $d$(D···A)/Å | $\langle$D–H···A/° |
|---|---|---|---|---|
| O5#6–H5A···N1 | 0.70(5) | 2.07(4) | 2.764(4) | 173(5) |
| O5#7–H5B···N3 | 0.93 | 2.08 | 2.771(3) | 130 |
| O(8)–H(8B)···O(4)#5 | 0.73(6) | 2.15(6) | 2.873(4) | 172(5) |
| N(2)–H(2A)···O(5) | 0.87(8) | 2.22(8) | 2.857(5) | 130(7) |

Note: Symmetry codes: #5: $-1 + x$, $0.5 - y$, $-0.5 + z$; #6: $1 - x$, $-0.5 + y$, $0.5 - z$; #7: $1 - x$, $1 - y$, $1 - z$.
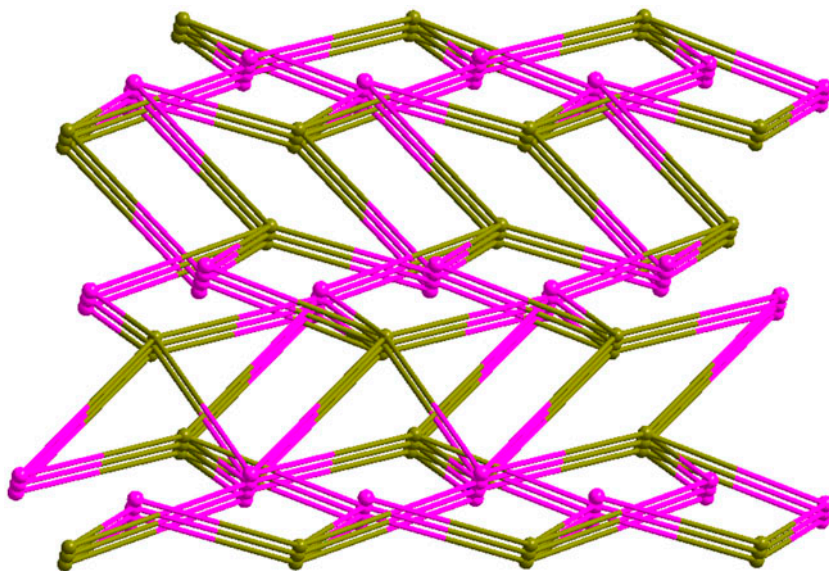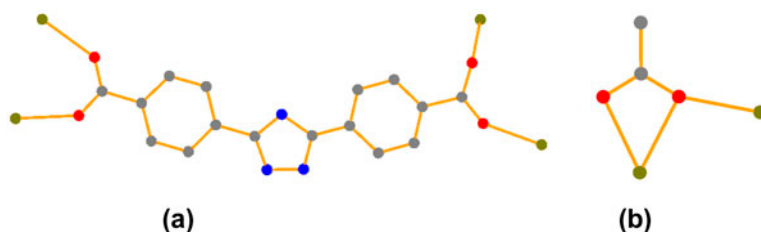


Figure 7.    The (4,4)-connected topological framework of **4**.

Scheme 1.   The coordination environments of BCPT$^{2-}$ (a) and OAc$^-$ (b).

fashion [scheme 1(b)] to form binuclear units. Thus, we can define the BCPT$^{2-}$ as four-connected and [Tb$_2$(CO$_2$)$_2$(O)$_2$] binuclear clusters also as four-connected. To analyze the net, the two equivalent nodes lead to a (4,4)-connected network (figure 7).

### 3.2.  Powder X-ray diffraction, IR, thermogravimetric analysis, and UV–visible spectra

The peak positions of experimental and simulated PXRD patterns for **1–6** are depicted in figure S2 and determined at room temperature. The experimental and simulated PXRD patterns are in agreement with each other, demonstrating good phase homogeneity and purity of **1–6**. The tiny difference in intensity may be due to the preferred orientation of the microcrystalline powder samples. The IR spectrum (figure S3) bands at 1305 and 1431–1694 cm$^{-1}$ in H$_2$BCPT ligand are characteristic of the C–O–C stretching vibrations of the CH$_2$–O–CPh and Ph–COOH groups. The strong bands at 1418–1614 cm$^{-1}$ of **1–6** are characteristic of the carboxyl groups. The broad and strong absorptions at 3070–3690 cm$^{-1}$ show the presence of water molecules in **1–6**. The thermal behaviors of **1–6** were explored by thermogravimetric analysis. The experiments were performed on **1–6** under air with a heating rate of 10 °C·min$^{-1}$, as shown in figure S4. The results reveal that **1–6** have similar thermal behavior; therefore, **4** is employed as a representative. For **4**, the initial mass loss of 6.2% (calculated: 6.4%) was observed from 80 to 270 °C, corresponding to loss of one lattice water as well as one coordinated water. Then, **4** experiences weight loss of 10.9% (calculated: 10.5%) from 300 to 410 °C, which is attributed to the decomposition of OAc$^-$. Finally, **4** starts to decompose upon further heating and weight loss above the temperature range of 410–800 °C, corresponding to destruction of BCPT$^{2-}$, and the final residue of 32.6% is close to the calculated value of 32.3% based on Tb$_2$O$_3$. Overall, the final products after thermal decomposition of **1–6** were rare earth oxides. The UV–visible spectra of H$_2$BCPT and its corresponding Ln$^{3+}$-MOFs **1–6** were recorded in the solid state, as shown in figure S5. H$_2$BCPT displays two main absorption maxima at 263 and 343 nm, which are assigned to singlet–singlet n–π* and π–π* absorptions of the aromatic rings, respectively. For **1–6**, single absorption maxima are 286, 289, 296, 294, 291, and 289 nm, respectively. The absorption profiles of **1–6** are not identical to that for free H$_2$BCPT, indicating coordination of Ln$^{3+}$ (Ln = Nd; Sm, Gd, Tb, Ho, Yb) ions does influence the energy of singlet states of H$_2$BCPT with a slight red shift, which can be attributable to the perturbation induced by Ln$^{3+}$ coordination.

### 3.3. *Luminescent properties of 1–4 and 6*

The luminescent properties of **1–4** and **6** have been investigated. Under excitation at 332 nm, when H$_2$BCPT ligand is introduced to sensitize Sm$^{3+}$ ion, **2** exhibits the typical emission bands of Sm$^{3+}$ in the spectral range of 550–700 nm (figure 8). The spectrum of **2** exhibits three emission bands at 553, 594, and 647 nm (assignable to the transitions: $^4G_{5/2} \to {}^6H_J$ ($J = 5/2$, 7/2, 9/2)). The emission at 647 nm is most intense. The excitation spectrum of **2** exhibits a broad and relatively weak band between 320 and 380 nm monitored at 647-nm transition, which can be assigned to $\pi$–$\pi$* electronic transition of H$_2$BCPT. Figure 9 presents the emission and excitation spectra of **4**. Upon excitation by UV light with 367 nm, **4** shows an emission spectrum with four characteristic emission bands at 487 nm ($^5D_4 \to {}^7F_6$), 545 nm ($^5D_4 \to {}^7F_5$), 582 nm ($^5D_4 \to {}^7F_4$), and 626 nm ($^5D_4 \to {}^7F_3$); the green emission of 545 nm is most intense. The excitation spectrum monitored at 545 nm, **4** shows a broad band between 350 and 420 nm with a maximum at 367 nm, which can be attributable to the $\pi$–$\pi$* electronic transition of the H$_2$BCPT ligand. The emission band of **4** from the H$_2$BCPT ligand is not detected, implying efficient energy transfer from the ligand to the Tb$^{3+}$ [15]. This result suggests that the H$_2$BCPT ligands are suitable for the sensitization of luminescence for Tb$^{3+}$ ion [16]. These observations are consistent with [Tb$_2$(L)$_6$(H$_2$O)$_4$]$_n$ [15] and {[Tb(HL)](H$_2$O)$_5$}$_n$ [16] (HL = 4-(dibenzylamino)-benzoic acid; H$_4$L = 1,3,5-triazine-2-iminodiacetic acid-4,6-bis), including the shape and characteristic emission bands (488, 545, 585, 620 nm for [Tb$_2$(L)$_6$(H$_2$O)$_4$]$_n$; 488, 545, 584, 622 nm for {[Tb(HL)](H$_2$O)$_5$}$_n$) of the emission spectrum.

To investigate the energy transfer mechanism of {[Ln(BCPT)(OAc)(H$_2$O)]·(H$_2$O)}$_n$ (Ln = Sm$^{3+}$ (**2**), Tb$^{3+}$ (**4**)), it is desirable to determine the energy levels of the relevant singlet and triplet excited states of H$_2$BCPT. The singlet energy level of H$_2$BCPT is calculated by UV–vis absorption spectrum of the complex for Gd$^{3+}$ and only BCPT$^{2-}$ ligand (figure S6),
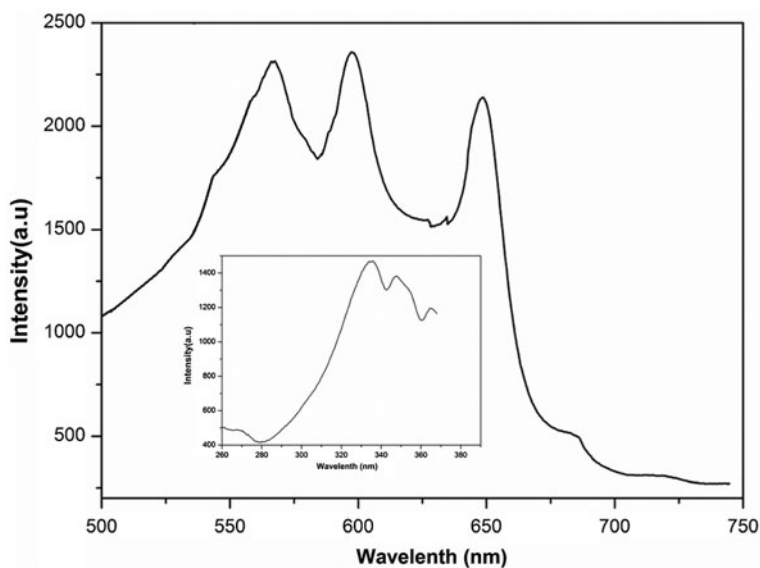


Figure 8.   Visible emission and excitation (inset) spectra of **2** in the solid state.
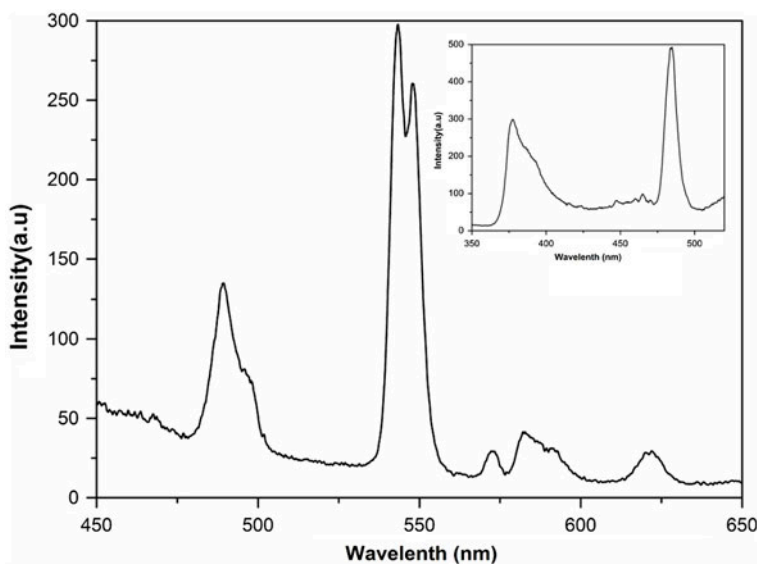
Figure 9. Visible emission and excitation (inset) spectra of **4** in the solid state.

and the relevant value of the $\pi\pi^*$ for H$_2$BCPT is 28,986 cm$^{-1}$ (345 nm). The triplet energy level for H$_2$BCPT is estimated by reference to the lower wavelength emission edge of the phosphorescence spectrum of Gd$^{3+}$ and BCPT$^{2-}$ (figure S7) at 77 K. Analysis of the phosphorescence emission shows that the value of the $^3\pi\pi^*$ for H$_2$BCPT is 23,256 cm$^{-1}$ (430 nm). Because the first excited state of Gd$^{3+}$ ($^6P_{7/2}$, 32,000 cm$^{-1}$) is too high to accept any energy from the first excited triplet state of the ligand through intramolecular ligand-to-metal energy transfer, the phosphorescence spectrum of the corresponding Gd$^{3+}$ compound (only BCPT$^{2-}$ ligand) could reveal the triplet energy level of the ligand. Figure 10 shows the diverse energy-level states of H$_2$BCPT, Sm$^{3+}$, and Tb$^{3+}$ with possible energy transfer pathways among them. The energy gap of the singlet state (28,986 cm$^{-1}$) and the triplet state (23,256 cm$^{-1}$) for H$_2$BCPT is 5730 cm$^{-1}$, being larger than 5000 cm$^{-1}$ and indicating that the intersystem crossing becomes effective according to Reinhoudt's empirical rule [17]. The triplet energy level of H$_2$BCPT lies above the resonant level of Sm$^{3+}$ (17,900 cm$^{-1}$) and Tb$^{3+}$ (20,500 cm$^{-1}$), allowing an efficient ligand-to-metal energy transfer. Latva's empirical rule states that an optimal ligand-to-metal energy transfer process for Tb$^{3+}$ requires $\Delta E$ = 2500–4500 cm$^{-1}$ and 2500–5000 cm$^{-1}$ for Sm$^{3+}$. The energy gap between the triplet state of H$_2$BCPT and $^5D_4$ state of Tb$^{3+}$ is 2756 cm$^{-1}$, suggesting that H$_2$BCPT could sensitize Tb$^{3+}$ emission in **4**. The energy gap between the triplet state of H$_2$BCPT and $^4G_{5/2}$ state of Sm$^{3+}$ is 5356 cm$^{-1}$, not an ideal situation for the sensitization of Sm$^{3+}$ luminescence.

As shown in figure 11, at the excitation wavelengths of 369 nm, **3** displays luminescent intensity. The emission spectra of the broad fluorescent emission band at 450–550 nm with $\lambda_{max}$ = 539 nm of **3** is assigned to ligand-centered fluorescence [18]. The excitation spectrum of **3** shows a broadband between 330 and 400 nm with a maximum at approximately 369 nm, which can be attributable to the $\pi$–$\pi^*$ electronic transition of H$_2$BCPT.

The Nd$^{3+}$ and Yb$^{3+}$ ions are luminescent in near-infrared spectral regions. However, compared with other complexes of Sm$^{3+}$, Eu$^{3+}$, Tb$^{3+}$, and Dy$^{3+}$ few efforts have been devoted to
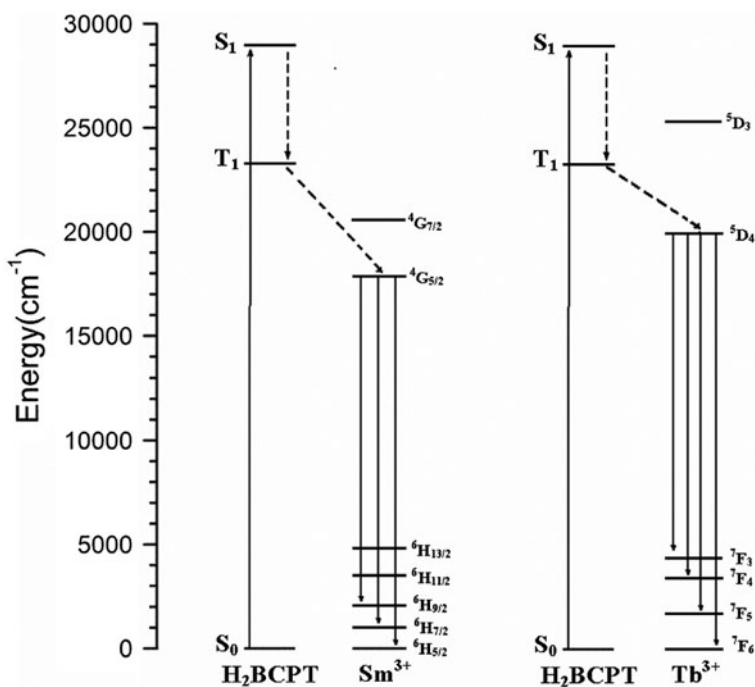
Figure 10. The diverse energy-level states of $H_2BCPT$, $Sm^{3+}$, and $Tb^{3+}$ and energy transfer pathways.
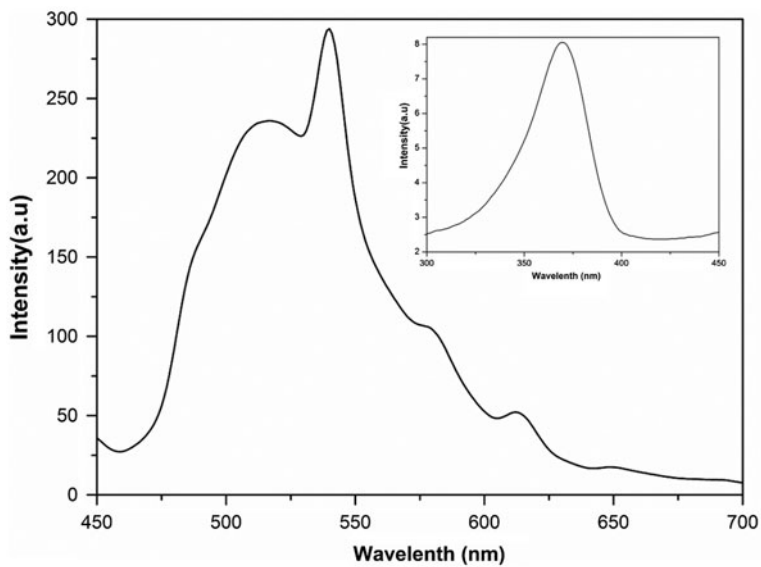


Figure 11. Visible emission and excitation (inset) spectra of **3** in the solid state.

research the fluorescence properties of $Nd^{3+}$-/$Yb^{3+}$-containing complexes. Complexes not only exhibit luminescent properties at 800–1400 nm, but also are studied in biological analysis, laser systems, etc. Therefore, the photoluminescence spectra of $Nd^{3+}$ and $Yb^{3+}$ complexes display typical narrow bands, as shown in figures 12 and 13. For **1**, upon 369-nm radiation excitation, the emission spectra consist of bands at 893, 1064, and 1337 nm in the near-infrared region which are attributed to the $^4F_{3/2} \rightarrow {}^4I_{9/2}$, $^4F_{3/2} \rightarrow {}^4I_{11/2}$, and $^4F_{3/2} \rightarrow {}^4I_{11/2}$
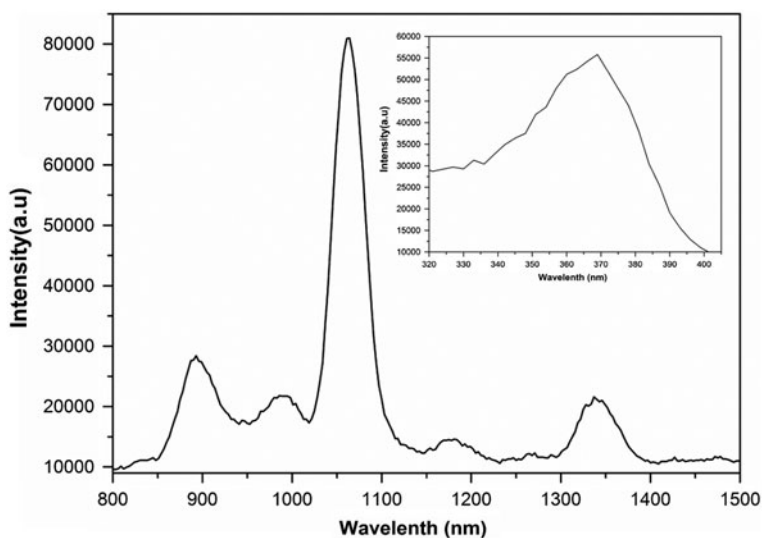
Figure 12. NIR emission and excitation (inset) spectra of **1** in the solid state.
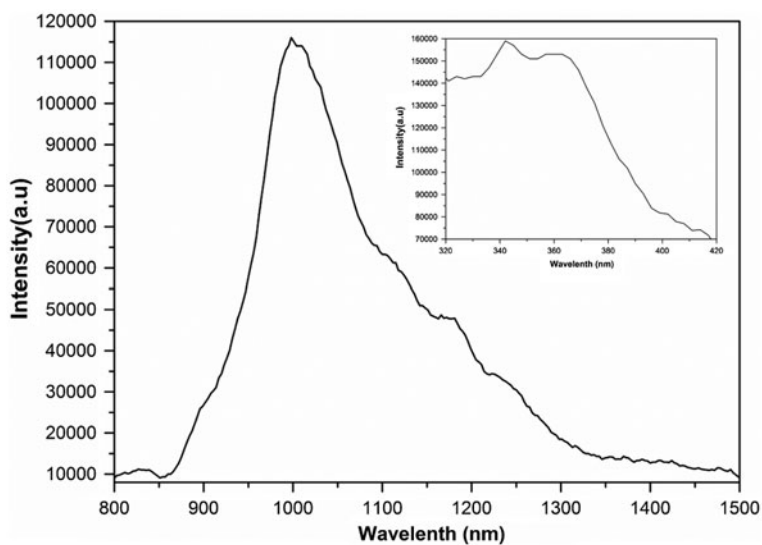


Figure 13. NIR emission and excitation (inset) spectra of **6** in the solid state.

transitions of $Nd^{3+}$ ions, respectively. The very strong emission band is at 1064 nm. For **6** at 342-nm radiation excitation, the emission spectrum contains one band at 998 nm corresponding to the $^2F_{5/2} \rightarrow {}^2F_{7/2}$ transition of $Yb^{3+}$ ion. The excitation spectra of **1** and **6**, monitored at the respective near-infrared emission peak (1064 nm for **1** or 998 nm for **6**), are similar to those monitored at their respective visible emission peaks, which clearly demonstrates that both the near-infrared and visible emissions for **1** and **6** originated from the same $\pi$–$\pi$* transitions of $H_2BCPT$. The sensitization of the near-infrared luminescence for **1** and **6** arise from both the 1LC (28,986 $cm^{-1}$) and the 3LC (28,986 $cm^{-1}$) excited state of $BCPT^{2-}$ [19].

## 4. Conclusion

A multidentate $H_2BCPT$ and HOAc have been utilized for the construction of six 3-D $Ln^{3+}$-MOFs; **1–6** are isomorphous with (4,4)-connected 3-D construction containing a dinuclear cluster unit $[Ln_2(CO_2)_2(O)_2]$. Solid-state photoluminescence properties of **1–4** and **6** were investigated. **2** exhibits bright orange luminescence, while **4** emits green luminescence, from characteristic f–f transitions of $Sm^{3+}$ and $Tb^{3+}$ ions. **3** displays luminescent intensity and is assigned to a ligand-centered fluorescence. MOFs **1** and **6** show the characteristic bands of $Nd^{3+}$ and $Yb^{3+}$ ions in near-infrared spectral regions. In contrast to lanthanide MOFs reported, the 2-D double-layer MOFs of [Nd(*trans*-DAM)(*cis*-DAM)(H$_2$O)$_2$]Cl·5H$_2$O [20] (DAM = dimethylammonium) which display emission spectra bands at 912, 1059, and 1333 nm; the 1-D MOFs for [Ln(pta)(H$_2$O)$_5$]·4H$_2$O [21] (Ln = Sm(**1**), Tb(**2**), Yb(**3**); pta = 2,4,6-pyridinetricarboxylate) exhibit emission bands at 558, 592, 639; 491, 546, 584, 623, and 546 nm, respectively, and the 3-D structures of [Gd$_2$(pyda)($\mu_4$-C$_2$O$_4$)$_2$·4H$_2$O]·3H$_2$O [22] (H$_2$pyda = 2,6-pyridine-dicarboxylic acid) exhibit emission at 980 nm. MOFs **1–6** present 3-D construction. This is due to the multidentate $BCPT^{2-}$ with $\mu_4$-$kO$;$kO$;$kO$;$kO$ coordination. We also investigated fluorescence properties from visible to near-infrared spectral regions about MOFs **1–4** and **6**. Further work on this subject is in progress.

## Disclosure statement

No potential conflict of interest was reported by the authors.

## References

[1] (a) X.Z. Song, S.Y. Song, C. Qin, S.Q. Su, S.N. Zhao, M. Zhu, Z.M. Hao, H.J. Zhang. *Cryst. Growth Des.*, **12**, 253 (2012); (b) Z.R. Herm, J.A. Swisher, B. Smit, R. Krishna, J.R. Long. *J. Am. Chem. Soc.*, **133**, 5664 (2011).

[2] (a) M.D. Allendorf, C.A. Bauer, R.K. Bhakta, R.J.T. Houk. *Chem. Soc. Rev.*, **38**, 1330 (2009); (b) Y.L. Wang, N. Zhou, Y. Ma, Z.X. Qin, Q.L. Wang, L.C. Li, P. Cheng, D.Z. Liao. *CrystEngComm*, **14**, 235 (2012); (c) Z.Q. Xia, Q. Wei, Q. Yang, C.F. Qiao, S.P. Chen, G. Xie, G.C. Zhang, C.S. Zhou, S.L. Gao. *CrystEngComm*,

**15**, 86 (2013); (d) D.S. Li, J. Zhao, Y.P. Wu, B. Liu, L. Bai, K. Zou, M. Du. *Inorg. Chem.*, **52**, 8091 (2013); (e) Q.R. Wu, J.J. Wang, H.M. Hu, Y.Q. Shangguan, F. Fu, M.L. Yang, F.X. Dong, G.L. Xue. *Inorg. Chem. Commun.*, **14**, 484 (2011); (f) L. Gou, Q.R. Wu, H.M. Hu, T. Qin, G.L. Xue, M.L. Yang, Z.X. Tang. *Inorg. Chim. Acta*, **361**, 1922 (2008); (g) M.H. He, C. Ji, Z.D. Shen, Q.Y. Li, G.W. Yang, W. Shen, Q.G. Qiou, X.F. Shen. *J. Coord. Chem.*, **66**, 1538 (2013); (h) G.B. Che, X.C. Wang, C.B. Liu, J. Chen, S.S. Wang, X.Y. Li. *J. Coord. Chem.*, **65**, 4185 (2012).

[3] (a) Y.L. Gai, K.C. Xiong, L. Chen, Y. Bu, X.J. Li, F.L. Jiang, M.C. Hong. *Inorg. Chem.*, **51**, 13128 (2012); (b) Y.H. Huang, Q.L. Zhu, T.L. Sheng, S.M. Hu, R.B. Fu, C.J. Shen, C.H. Tan, Y.H. Wen, S.Y. Bai, X.T. Wu. *CrystEngComm*, **15**, 3560 (2013).

[4] S.I. Klink, G.A. Hebbink, L. Grave, P.G.B. Oude Alink, F.C.J.M. van Veggel, M.H.V. Werts. *J. Phys. Chem. A*, **3681**, 106 (2002).

[5] E.G. Moore, A.P.S. Samuel, K.N. Raymond. *Acc. Chem. Res.*, **42**, 542 (2009).

[6] (a) J.W. Ye, Q.Q. Wang, H.Z. Gao, X.Y. Lu, W.T. Gong, Y. Lin, G.L. Ning. *Inorg. Chim. Acta*, **384**, 1 (2012); (b) G. Bozoklu, C. Marchal, J. Pécaut, D. Imbert, M. Mazzanti. *Dalton Trans.*, **39**, 9112 (2010); (c) B.V. Harbuzaru, A. Corma, F. Rey, J.L. Jordá, D. Ananias, L.D. Carlos, J. Rocha. *Angew. Chem. Int. Ed. Engl.*, **48**, 6476 (2009).

[7] (a) S.Q. Su, S. Wang, X.Z. Song, S.Y. Song, C. Qin, M. Zhu, Z.M. Hao, S. Zhao, H.J. Zhang. *Dalton Trans.*, **41**, 4772 (2012); (b) S.T. Zheng, T. Wu, C.T. Chou, A. Fuhr, P.Y. Feng, X.H. Bu. *J. Am. Chem. Soc.*, **134**, 4517 (2012); (c) F.M. Zhang, P.F. Yan, X.Y. Zou, J.W. Zhang, G.F. Hou, G.M. Li. *Cryst. Growth Des.*, **14**, 2014 (2014).

[8] (a) K. Miyata, T. Ohba, A. Kobayashi, M. Kato, T. Nakanishi, K. Fushimi, Y. Hasegawa. *ChemPlusChem*, **77**, 277 (2012); (b) H.F. Li, P.F. Yan, P. Chen, Y. Wang, H. Xu, G.M. Li. *Dalton Trans.*, **41**, 900 (2012).

[9] T.H. Zhou, F.Y. Yi, P.X. Li, J.G. Mao. *Inorg. Chem.*, **49**, 905 (2010).

[10] F.Y. Yi, Q.P. Lin, T.H. Zhou, J.G. Mao. *Cryst. Growth Des.*, **10**, 1788 (2010).

[11] G.M. Sheldrick. *SHELEXS 97, Program for Crystal Structure Solution*, University of Gottingen, Gottingen, Germany (1997).

[12] G.M. Sheldrick. *SHELXXS 97, Program for Refinement of Crystal Structure*, University of Gottingen, Gottingen, Germany (1997).

[13] (a) P.F. Shi, Z. Chen, G. Xiong, B. Shen, J.Z. Sun, P. Cheng, B. Zhao. *Cryst. Growth Des.*, **12**, 5203 (2012); (b) X. Wang, Q.G. Zhai, S.N. Li, Y.C. Jiang, M.C. Hu. *Cryst. Growth Des.*, **14**, 177 (2014).

[14] H.L. Sun, X.L. Wang, L. Jia, W. Cao, K.Z. Wang, M. Du. *CrystEngComm*, **14**, 512 (2012).

[15] A.R. Ramya, M.L.P. Reddy, A.H. Cowley, K.V. Vasudevan. *Inorg. Chem.*, **49**, 2007 (2010).

[16] Y.H. Huang, Q.L. Zhu, T.L. Sheng, S.M. Hu, R.B. Fu, C.J. Shen, C.H. Tan, Y.H. Wen, S.T. Bai. *CrystEngComm.*, **15**, 3560 (2013).

[17] F.J. Steemers, W. Verboom, D.N. Reinhoudt, E.B. van der Tol, J.W. Verhoeven. *J. Am. Chem. Soc.*, **117**, 9408 (1995).

[18] R.E. Sykora, P. Khalifah, Z. Assefa, T.E. Albrecht-Schmitt, R.G. Haire. *J. Solid State Chem.*, **181**, 1867 (2008).

[19] W.X. Feng, Y. Zhang, X.Q. Lü, Y.N. Hui, G.X. Shi, D. Zou, J.R. Song, D.D. Fan, A.K. Wong, R.A. Jones. *CrystEngComm*, **14**, 3456 (2012).

[20] X.C. Chai, Y.Q. Sun, R. Lei, Y.P. Chen, S. Zhang, Y.N. Cao, H.H. Zhang. *Cryst. Growth Des.*, **10**, 658 (2010).

[21] H.S. Wang, B. Zhao, B. Zhai, W. Shi, P. Cheng, D.Z. Liao, S.P. Yan. *Cryst. Growth Des.*, **7**, 1851 (2007).

[22] X. Feng, L.Y. Wang, J.S. Zhao, J.G. Wang, N.S. Weng, B. Liu, X.G. Shi. *CrystEngComm*, **12**, 774 (2010).